

Article

Real-time morphometric analysis of targeted therapy for neuroblastoma cells in monolayer and 3D hydrogels using digital holographic microscopy

High Risk Neuroblastoma cell lines

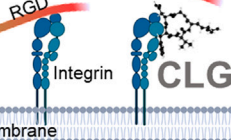
SK-N-BE(2)  SH-SY5Y 

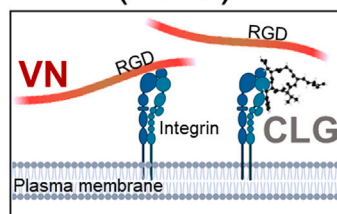
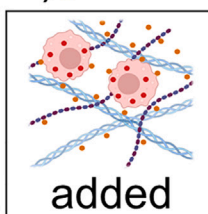
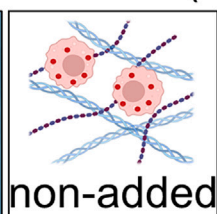
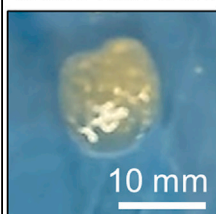
3D hydrogel scaffolds

Gelatin-
Silk fibroin

Vitronectin
(VN) 

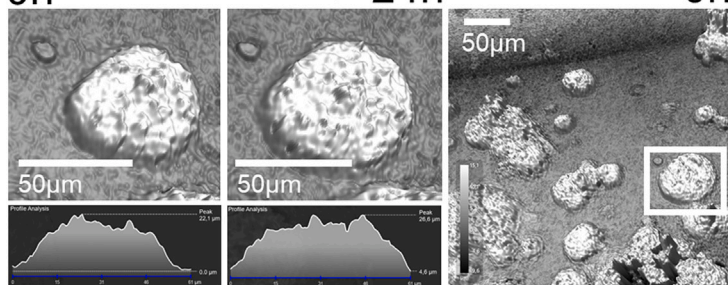
Drug testing

Cilengitide
(CLG) 



Real-time morphometric analysis

0h -----> 24h 0h



Sofia Granados-Aparici, Isaac Vieco-Martí, Amparo López-Carrasco, Samuel Navarro, Rosa Noguera

sgranados@incliva.es (S.G.-A.)
rnoguera@uv.es (R.N.)

Highlights

Digital holography enables the assessment of neuroblastoma cell dynamics

Vitronectin enhances cluster growth rate inside 3D hydrogels

Cilengitide promotes cell aggregation in cell monolayers and 3D hydrogel borders

Real-time monitoring of 3D models is a valuable tool for precision medicine

Granados-Aparici et al.,
iScience 27, 111231
November 15, 2024 © 2024 The Authors. Published by Elsevier Inc.
<https://doi.org/10.1016/j.isci.2024.111231>

Article

Real-time morphometric analysis of targeted therapy for neuroblastoma cells in monolayer and 3D hydrogels using digital holographic microscopy

Sofia Granados-Aparici,^{1,2,*} Isaac Vieco-Martí,^{1,2} Amparo López-Carrasco,^{1,2} Samuel Navarro,^{1,2} and Rosa Noguera^{1,2,3,*}

SUMMARY

High-risk neuroblastoma (HR-NB) patient treatment is currently insufficient and challenging due to its high clinical, morphological, and genetic heterogeneity as well as the scarcity of available samples for research. We used a gelatin- and silk fibroin-based hydrogel system with cross-linked vitronectin (VN) as an artificial biomimetic three-dimensional (3D) environment to mirror aggressive neuroblastoma (NB) tumors and tested long-term cell response to Cilengitide (CLG). Based on our previous studies and others using the integrin inhibitor CLG as a potential mechanotherapy drug, we show that CLG caused cell detachment in monolayer cultures of MYCN-amplified SK-N-BE (2) and ALK-mutated SH-SY5Y human neuroblastoma cell lines. Cell detachment and aggregation were maintained in hydrogel-free monolayer cells whereas cells embedded in hydrogels presented different responses to treatment, suggesting differential anoikis resistance between the two cell lines. This underscores the advantages of testing therapeutic approaches using real-time imaging of tumor cells in 3D biomimetic models and its contribution to precision medicine.

INTRODUCTION

Neuroblastoma (NB) is the most common extra-cranial solid tumor of childhood.¹ The survival rate in patients with low- and intermediate-risk disease is around 85%, and the 5-year survival rate for high-risk (HR) NB patients is less than 50%.² Treating HR-NB patients is challenging since they present high heterogenic clinic and tumor biology. To date, the combined use of chemotherapy, surgery, stem cell transplant, radiotherapy, and immunotherapy (anti-GD2) has been the most appropriate therapeutic approach.³ However, this combination is still insufficient and causes side effects that often appear as patients get older. Pilot studies are therefore needed to seek new targets and therapeutic approaches, such as molecular mechanotherapy.^{4,5}

The tumor microenvironment (TME) plays an important role in tumor progression, invasion, metastasis, and therapeutic resistance and is formed by elements such as the extracellular matrix (ECM), consisting of a dynamic network of structural proteins, glycoproteins, and proteoglycans^{6,7} that connect to cells and are essential for mechanotransduction.⁸ Vitronectin (VN) is a cell-ECM anchorage glycoprotein that interacts strongly with integrins $\alpha v\beta 3/\alpha v\beta 5$, uPAR, PAI-1, and collagens via the arginylglycylaspartic acid (RGD), heparin, somatomedin B, and two collagen-binding domains,^{9–11} therefore promoting tissue component adhesion. As an ECM tissue component, predominantly secreted into the bloodstream by hepatocytes, VN is mainly expressed in the liver and in smaller amounts in the ECM of the brain, lung, kidney, and adrenal gland.^{12,13} Dual sources of VN in human cancer biopsies have been described: extravasation from the bloodstream followed by ECM accumulation^{14–16} and/or synthesis and secretion by malignant cells and/or tumor-derived fibroblast-like cells.^{17–21} In the NB setting, previous studies of NB patient biopsies found high VN expression levels in the cytoplasm of malignant neuroblasts and in the ECM, which were associated with poor patient outcome.^{22,23} A recent study has also reported high VN levels in plasma of NB patients and culture media of 3D models.²⁴ These results point to the potential of this protein as a circulating ECM biomarker for aggressiveness in HR-NB. Cilengitide (EMD 121974, CLG) is a mechanodrug based on the cyclic peptide cyclo(-RGDfV-), selective for $\alpha v\beta 3$ and $\alpha v\beta 5$ integrins. Although CLG showed moderate anti-tumor effects in glioblastoma phase 1 and 2 clinical trials, this was mainly attributed to high heterogeneity in $\alpha v\beta 3$ levels, unfavorable drug pharmacokinetics, and its dose-dependent opposing effects.²⁵ Despite these results, CLG and other integrin inhibitors are still in the spotlight for treatment of pediatric and adult cancers,²⁶ and indeed *in vitro* assessment and preclinical models have shown antiangiogenic, cytotoxic, and anti-invasive activities.²⁷ Studies specifically assessing the effect of CLG in NB cells are few in number and consist mainly of *in vitro* short-term evaluations in monolayer cultures.^{28–30}

¹Pathology Department, Medical School, University of Valencia-INCLIVA, Valencia, Spain

²Centro de Investigación Biomédica en Red de Cáncer, Instituto de Salud Carlos III, 28029 Madrid, Spain

³Lead contact

*Correspondence: sgranados@incliva.es (S.G.-A.), rnoguera@uv.es (R.N.)

<https://doi.org/10.1016/j.isci.2024.111231>



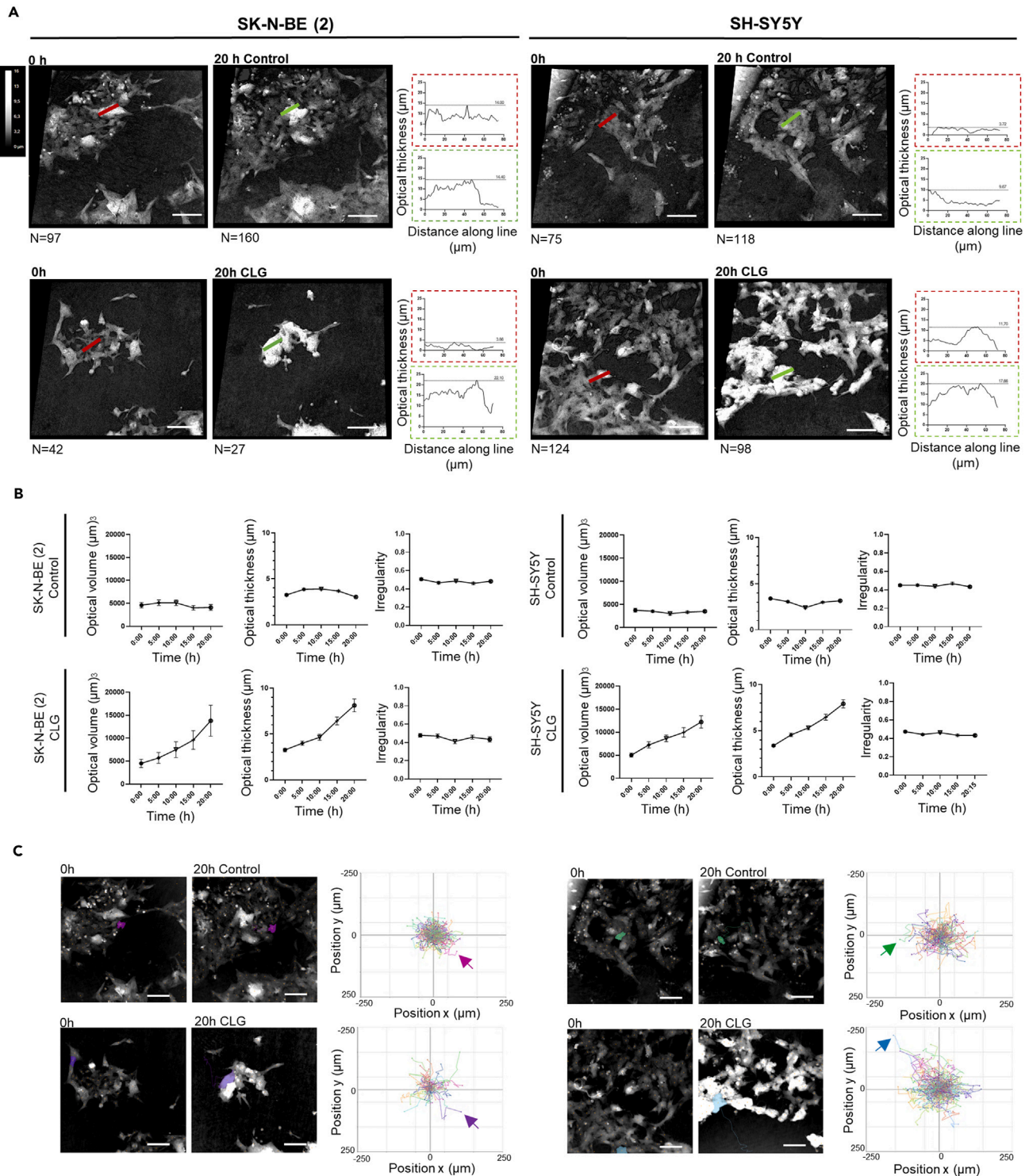


Figure 1. Growth rate morphometric parameters and movement pattern of SK-N-BE (2) and SH-SY5Y cells in monolayer cultures with and without CLG
(A) Holographic micrographs of a representative focus position obtained at 0 h and 20 h with and without CLG treatment of SK-N-BE (2) (right) and SH-SY5Y (left) cells. The small inset graph represents the optical thickness of the cell aggregate measured along the red and green lines in control and CLG treatment groups, respectively. The dotted line shows the maximum thickness in each graph. The number of cells is N = 97 (0 h) and N = 150 (24 h) in SK-N-BE (2) and N = 75 (0 h) and N = 118 (24 h) in SH-SY5Y.

(B) Measurement over time of optical volume (μm^3), optical thickness (μm), and irregularity (0 = smooth, 1 = rough) of cell micrographs shown in (A).

Figure 1. Continued

(C) Movement of the highlighted cell with long-distance trajectory from each micrograph in control and CLG treatment groups. Rose plots depict relative single-cell tracking X-Y migration showing the similarities (more symmetry) and differences (less symmetry) in movement from all cells. Arrows highlight the movement of the depicted cell.

The field of view is 567 × 567 μm. The scale bar is 100 μm. Brighter color represents maximum cell height. CLG, Cilengitide.

NB is a rare tumor, and scarcity of samples is a reality in research. The use of three-dimensional (3D) artificial tumors represents an efficient strategy to recreate tissue structure²³ and study NB in detail. SK-N-BE (2) and SH-SY5Y neuroblastic cell lines, which express VN in 70% of their cells with different staining intensity (+++/++), have been efficiently grown in Polyethylene glycol (PEG)- and methacrylated gelatin/alginate (GelMaAlgM)-based hydrogels.^{31,32} Recently, silk fibroin (sf) has emerged as a promising material for its excellent self-assembly, biocompatibility, and biodegradation, and the combination of sf with gelatin-tyramine (GTA-sf hydrogels) has shown high crosslinking capacity to any tyrosine-rich element such as VN,³³ providing a potential 3D biomimetic *in vitro* testing platform to help identify patient-specific therapeutic responses.

Developing detailed image analysis pipelines using digital pathology of histological slides has become essential to study the complex behavior of tumor cells in a spatial-temporal context.³⁴ However, specimen sections are static snapshots, and specific molecular biomarkers are needed to better assess cell death, proliferation, and migratory activity. The advent of real-time technologies is proving key to more comprehensively depicting underlying cell dynamics and response to different ECM environments and mechanotherapies. Holographic imaging (HoloMonitor M4, PhI Ab) has emerged as a potential live-cell tracking tool to monitor 3D dynamic behaviors including single-cell motilities, cell-cell interactions, and cell-surface interactions inside the CO₂ incubator.^{35,36} This resource has been increasingly used over the last decade (<https://phiab.com/peer-reviewed-publications/>) to follow cultured cells and assess changes in size, movement, and migration without perturbing viability since it permits label-free imaging and the low-energy laser keeps phototoxicity to a minimum.

In this work, we used digital holographic microscopy to characterize the morphometric changes of two NB cell lines, SK-N-BE (2) and SH-SY5Y, in response to CLG. Moreover, by crosslinking ECM components such as VN to GTA-sf hydrogels, we assessed and compared this response in 3D VN-rich hydrogels as representative of aggressive HR-NB environments, with the aim of developing a potentially translational *in vitro* drug-testing methodology for precision medicine.

RESULTS**Short-term CLG treatment induces rapid cell aggregation in monolayer cultures**

We followed the growth rate, irregularity, and movement patterns in monolayer cultures of SK-N-BE (2) and SH-SY5Y human NB cell lines during a short-term, 20 h culture treatment (Video S1). When untreated cells divide, they proliferate to reach cell confluency, filling the spaces available from the substrate. If space is not available, a few small cell aggregates are formed over time. In contrast, we observed that CLG-treated cells mainly aggregated independently of existing space. When optical thickness was measured in a representative cluster from control and CLG-treated cells after 20 h of live cell tracking (Figure 1A), increased thickness was observed along the surface of CLG-treated cell aggregates compared to controls over time, reaching a maximum of 22.10 μm (SK-N-BE-2) and 17.66 μm (SH-SY5Y) at 20 h, in contrast to the 14.4 μm (SK-N-BE-2) and 9.67 μm (SH-SY5Y) of controls. This was observed in various cell aggregates in both NB cell lines and in replicated experiments using CLG treatment (Video S2). Interestingly, the number of cells in both cell lines counted at 0 h and 20 h increased over time in control conditions, whereas a decrease was observed in CLG-treated cells, as shown by the higher proportion of cell clusters counted as "1" by the App Suite software (Figure 1A). While cells in control conditions grew to cover the spaces available from the focus position, cells treated with CLG preferred to cluster together despite the availability of space. This was further evidenced by measuring the cell-free area available at 0 h and 20 h of treatment (Figure S1A). Over time (20 h), the average cluster optical volume and thickness for both NB cell lines showed a steady increase in CLG-treated cells, whereas control cells maintained a plateau. Irregularity remained unchanged in both cell lines and conditions (Figure 1B). We obtained the relative trajectory profile of detected cells where the position of each cell is normalized by its initial position (Figure 1C). A rose plot was generated in which a more symmetric plot indicates similar movement patterns between cells. In contrast to the symmetric profile observed in cells growing in control conditions, cells growing with CLG showed less symmetry in their movement pattern and some cells reached longer distances than others with slightly higher motility speed across 20 h (Figure 1B). When following a cell with a long-distance trajectory from each condition over time, we observed that cells in control conditions changed their position toward an empty space, whereas cells in CLG conditions tended to move toward pre-existing cell clusters (Figure 1C). These results suggest that NB cells in CLG conditions tend to join to neighboring cells rather than attaching to the substrate.

Long-term CLG treatment maintains cell aggregation at the 3D GTA-sf hydrogel border

We optimized a culture system for NB cells in 3D GTA-sf hydrogels as specified in the STAR Methods. This methodology allows us to study NB cell growth over longer periods of time and to introduce specific ECM components like VN into the scaffolds due to the previously mentioned chemical characteristics of GTA. During hydrogel-induced gelation, some cells are usually not retained and start to grow besides the hydrogel. This allows us to monitor cell growth in 3D and in monolayers simultaneously. Since GTA-sf hydrogels were monitored for up to 10 days in culture, we studied the effect of long-term CLG treatment in monolayered cells located just outside the hydrogel (Figure 2). Cell aggregates continued to be observed in CLG-treated groups at the hydrogel border in both NB cell lines, whereas a dense flat monolayer was present in control groups (Figure 2A). Moreover, the number of cells detected was lower in CLG-treated groups, correlating with cell aggregation rather than spread through the available spaces. When the relative trajectories of cells outside the hydrogels were plotted (Figure 2B), CLG-treated

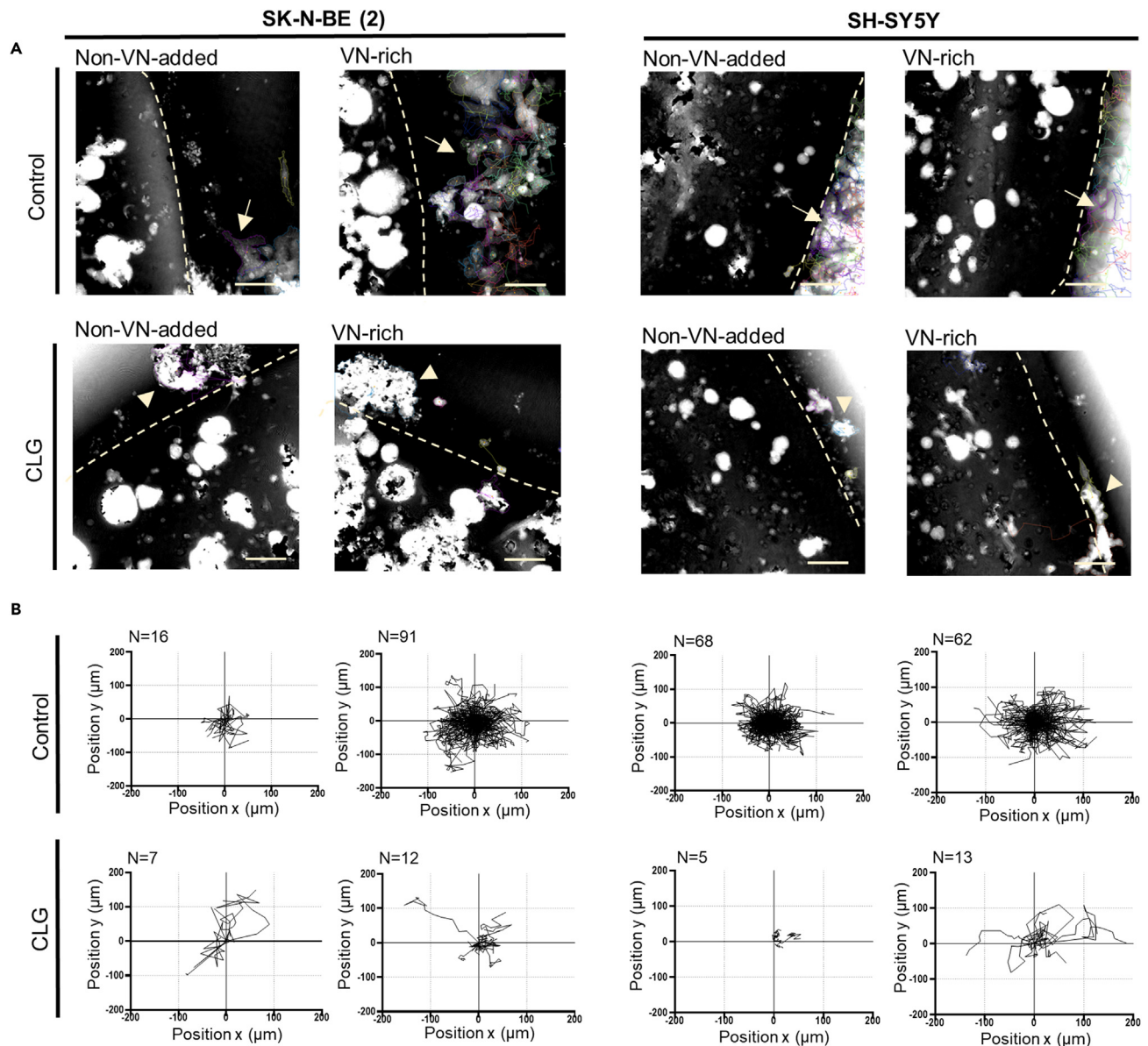


Figure 2. Long-term movement pattern in hydrogel-free 2D-grown SK-N-BE (2) and SH-SY5Y cell lines at the hydrogel border with and without CLG
(A) Representative holographic micrographs from hydrogel-grown SK-N-BE (2) (right) and SH-SY5Y (left) cell lines with selected hydrogel-free-grown cells at the non-VN-added and VN-rich hydrogel border at day 10 of culture (time point: 24 h). Arrows and arrow heads highlight cells growing in monolayer and cell aggregates, respectively. The border is highlighted with a dotted line.
(B) Rose plots depict relative single-cell tracking X-Y migration showing the similarities (more symmetry) and differences (less symmetry) in cell movement of all selected cells from up to three different focus positions from each condition. The field of view is $567 \times 567 \mu\text{m}$. The scale bar is $100 \mu\text{m}$. CLG, Cilengitide; VN, vitronectin.

clusters showed asymmetric rose plots representing cell aggregates moving longer distances than others in contrast to control groups, which followed a more symmetric movement pattern. Interestingly, cell aggregates often moved toward the surface of the hydrogel (Video S3), which may be the result of a search for optimal attachment. Altogether, these observations confirm that the effect of densely packed cell aggregate formation after CLG treatment is maintained after long periods of time without spreading for both NB cell lines.

NB cell lines show different cluster size dynamics over time inside GTA-sf hydrogels

We assessed cell growth inside GTA-sf hydrogels, first detecting a switch toward round cell cluster formation, as previously described in our PEG- and GelMaAlgM-based hydrogels. Next, clusters inside the GTA-sf hydrogel border were analyzed at days 3, 7, and 10 of culture using

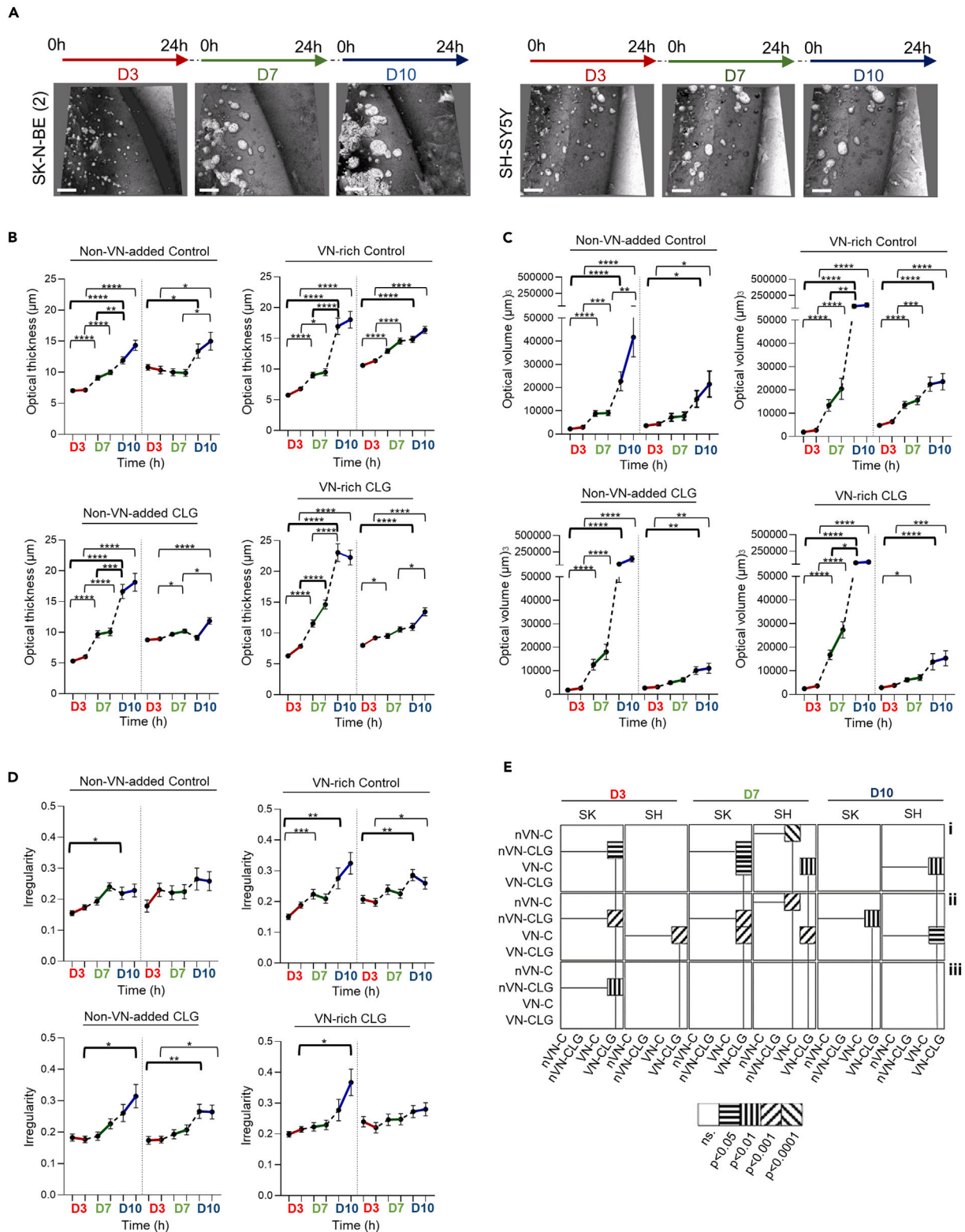


Figure 3. Comparison of cluster morphometric parameters of SK-N-BE (2) and SH-SY5Y cells over 3, 7, and 10 days of culture in non-VN-added and VN-rich 3D GTA-sf hydrogels with and without CLG

(A) Representative holographic micrographs from VN-rich hydrogel-grown SK-N-BE (2) and SH-SY5Y cell clusters without CLG at day 3, 7, and 10 of culture. Red, green, and blue arrows depict the 24 h-length videos taken at 0 and 24 h.
 (B–D) Morphometric parameters in SK-N-BE (2) and SH-SY5Y cell clusters at 0 h and 24 h of day 3 (red line), 7 (green line), and 10 (blue line) time points in non-VN-added and VN-rich hydrogels without CLG (upper graphs) and with CLG (lower graphs). (B) Optical volume (μm^3), (C) optical thickness (μm), and (D) irregularity (0–1) measurements. Data are represented as mean \pm SEM.
 (E) Heatmap of statistically significant differences of SK-N-BE (2) and SH-SY5Y cell clusters at 3, 7, and 10 day time points between non-VN-added and VN-rich hydrogels without CLG and with CLG. (i) Optical volume (μm^3), (ii) optical thickness (μm), and (iii) irregularity (0–1) measurements. SK: SK-N-BE (2), SH: SH-SY5Y, nVN-C: non-VN-added Control, nVN-CLG: non-VN-added CLG, VN-C: VN-rich-Control, VN-CLG: VN-rich-CLG. Statistical analysis using non-parametrical Kruskal-Wallis test, * $p < 0.05$; ** $p < 0.01$; *** $p < 0.001$; **** $p < 0.0001$. SEM, standard error of the mean. Significant differences discussed in the text are highlighted in bold. The field of view is $567 \times 567 \mu\text{m}$. The scale bar is $100 \mu\text{m}$. D, day, CLG, Cilengitide, VN, vitronectin.

optical volume, thickness, and irregularity parameters in the two VN amount-dependent hydrogels or scaffoldings (non-VN-added and VN-rich) without CLG treatment. Increased cluster size across culture time was observed in both NB cell lines (Figures 3A and S2A). However, while cluster volume and thickness increased abruptly from day 7 (0 h) to day 10 of culture (0 h) in both VN scaffoldings in the SK-N-BE (2) cell line (VN-rich, mean volume = $13,359 \mu\text{m}^3$ vs. $10,0785 \mu\text{m}^3$; $p = 0.0208$; non-VN-added, mean thickness = $9.09 \mu\text{m}$ vs. $11.90 \mu\text{m}$; $p = 0.0081$; VN-rich, mean thickness = $9.00 \mu\text{m}$ vs. $16.94 \mu\text{m}$; $p < 0.0001$), this increase was steady and less pronounced in SH-SY5Y cells, without reaching statistical significance (Figures 3B and 3C, upper graphs). In contrast, when measuring irregularity, a similar steady increase was observed for the two NB cell lines (Figure 3D, upper graphs), although at day 10 of culture in VN-rich conditions, SK-N-BE (2) showed higher irregularity (0–1) than SH-SY5Y cells (24 h, mean irregularity = 0.32 vs. 0.25, respectively) (Figure 3D). Next, cluster volume and thickness were compared between non-VN-added and VN-rich conditions to assess the impact of the VN scaffoldings over time. We observed an increase in cluster volume and thickness in VN-rich hydrogels compared with non-VN-added hydrogels in SK-N-BE (2) cells at days 7 and 10 (Figures 3B and 3C, upper graphs), although without reaching statistical significance (Figures 3E and 3Ei and 3Eii), whereas in the SH-SY5Y cell line the same parameters (Figures 3B and 3C, upper graphs) exhibited a significant increase in VN-rich relative to non-VN-added conditions at days 3 and 7 of culture (Figures 3E and 3Ei and 3Eii). A significant increase in cluster irregularity in VN-rich hydrogels was observed from day 3 (0 h) to day 10 (0 h) of culture in both NB cell lines (Figure 3D, upper graphs). This increase was particularly evident at day 10 of culture in SK-N-BE (2) cells (mean irregularity = 0.32 vs. 0.22, respectively) (Figure 3D, upper graphs), although without reaching statistical significance (Figures 3E and 3Eiii). These results indicate that NB cell lines experience optimal growth during 10 days in GTA-sf hydrogels, although with different growth dynamics. Moreover, VN accelerates the growth rate of both NB cell lines, as evidenced by the observed increase in cluster volume, thickness, and irregularity associated with this event.

NB cell lines respond differently after CLG treatment inside GTA-sf hydrogels

We next sought to investigate the effect of CLG treatment on cluster size inside GTA-sf hydrogels at days 3, 7, and 10 of culture. As observed with the non-VN-added and VN-rich control conditions, increased cluster size over time was observed in both NB cell lines treated with CLG, with the SK-N-BE (2) cell line showing a more abrupt increase over time than SH-SY5Y cells (Figures 3A and 3B, lower graphs). A similar steady increase was observed in cluster irregularity for the two NB cell lines (Figure 3D, lower graphs), with higher values in the SK-N-BE (2) cell line than in SH-SY5Y cells at day 10 of culture in VN-rich hydrogels with CLG (mean irregularity = 0.36 vs. 0.28, respectively) (Figure 3D). However, we observed a difference in time-related response to CLG treatment between the specific scaffoldings in the NB cell lines (Figure 3E). Analysis of VN-rich hydrogels showed that SK-N-BE (2) clusters treated with CLG increased significantly in volume and thickness relative to their untreated control counterparts, but only at day 7 of culture (24 h, mean volume = $27,326 \mu\text{m}^3$ vs. $15,543 \mu\text{m}^3$, $p = 0.0093$; 24 h, mean thickness = $14.64 \mu\text{m}$ vs. $9.485 \mu\text{m}$; $p < 0.0001$) (Figures 3E and 3Ei and 3Eii), whereas in SH-SY5Y cells a significant decrease was observed at all time points (day 3 [24 h, mean thickness = $9.21 \mu\text{m}$ vs. $11.35 \mu\text{m}$, $p < 0.0001$], day 7 [24 h, mean volume = $7,132 \mu\text{m}^3$ vs. $15,543 \mu\text{m}^3$; $p = 0.04$; 24 h, mean thickness = $10.59 \mu\text{m}$ vs. $14.55 \mu\text{m}$, $p < 0.0001$], and day 10 [24 h, mean volume = $13,840 \mu\text{m}^3$ vs. $15,331 \mu\text{m}^3$; $p = 0.04$], [24 h, mean thickness = $11.00 \mu\text{m}$ vs. $14.82 \mu\text{m}$, $p = 0.01$]) (Figures 3E and 3Ei and 3Eii). Comparing the non-VN-added and VN-rich conditions after CLG treatment on specific days, SK-N-BE (2) cells showed a significant increase in volume and thickness at day 3 (24 h, mean volume = $2,583 \mu\text{m}^3$ vs. $3,607 \mu\text{m}^3$, $p = 0.0057$; 24 h, mean thickness = $6.00 \mu\text{m}$ vs. $7.84 \mu\text{m}$; $p < 0.0001$), day 7 (24 h, mean volume = $18,034 \mu\text{m}^3$ vs. $27,326 \mu\text{m}^3$, $p = 0.0061$; 24 h, mean thickness = $10.06 \mu\text{m}$ vs. $14.64 \mu\text{m}$; $p < 0.0001$), and day 10 of culture (24 h, mean thickness = $10.06 \mu\text{m}$ vs. $14.64 \mu\text{m}$; $p < 0.0001$) (Figures 3E and 3Ei and 3Eii). In contrast, SH-SY5Y cells showed no differences at any of the time points (Figures 3E and 3Ei and 3Eii). With respect to changes in irregularity, similar increases over time were observed in SK-N-BE (2) with CLG treatment, but in SH-SY5Y cells this increase in VN-rich hydrogels lost significance from day 3 (0 h) to day 10 (0 h) of culture (Figure 3D, lower graphs). Comparing non-VN-added and VN-rich conditions after CLG treatment at specific time points, increased irregularity was evident in SK-N-BE (2) cells at day 3 of culture (24 h, mean irregularity = 0.17 vs. 0.21; $p = 0.0498$). An increasing trend was also observed in these cells at day 10 of culture (24 h) in non-VN-added hydrogels with CLG compared with non-VN-added controls (mean irregularity = 0.31 vs. 0.22) (Figure 3D, lower graphs), reaching similar values as in VN-rich conditions (VN-rich CLG vs. control, mean irregularity = 0.36 vs. 0.32) without statistical significance (Figures 3E and 3Eiii). Altogether, these findings suggest that both NB cell lines respond to CLG treatment compared to untreated controls. Although the response is different for each cell type, it is often accentuated in VN-rich conditions.

DISCUSSION

We employed digital holographic microscopy to examine the effect of CLG on NB cells grown in monolayers as well as inside 3D GTA-sf hydrogels and its borders. Preclinical therapeutic studies by our group have reported a direct anticancer activity of CLG in HR-NB cell monolayer cultures and showed its synergy with free and nano-encapsulated etoposide (ETP), particularly in SK-N-BE (2) cells.³⁰ Moreover, a synergic reduction in tumor volume and VN expression was observed in a small trial with murine models of NB treated with CLG and ETP combined.³⁷ However, until now the morphological effect of CLG alone on NB cells *in vitro* and the response in GTA-sf hydrogels have remained uncharacterized.

Our detailed study of the effect of CLG using short-term exposure in NB monolayer cultures revealed cell detachment and aggregation, a phenotype previously described for NB and pediatric glioma cell lines using CLG,^{29,38} suggesting the possibility of anoikis (cell detachment-associated cell death). Similarly, the CLG-induced cell detachment observed in this work during 20 h of monolayer culture could precede NB cell death. To study long-term exposure to CLG, we followed cells grown outside the GTA-sf hydrogels during 10 days of culture. While a dense monolayer was observed covering the empty spaces from the substrate in controls, cells in CLG-treated groups showed a few aggregates that migrated over the hydrogel surface. The persistence of cell aggregation in small numbers without cell confluency may suggest that cell detachment in NB cell lines results in decreased cell growth in addition to the classical cytotoxic effect triggered by anoikis.

When comparing environments with only the VN secreted by cells (non-VN-added) versus those with added VN (VN-rich) in GTA-sf hydrogels, clusters increased in size with the addition of VN, suggesting that this protein could enhance proliferation over cell death similarly in both NB cell lines, concurring with as has been previously reported.^{17,39,40} However, in CLG-exposed GTA-sf hydrogel-embedded cells, cluster size showed different time-dependent dynamics in the two NB cell lines studied. It is well known that cancer cells develop anoikis resistance due to several mechanisms that enhance cancer progression and metastasis.^{41,42} Within cell clusters, leader cells initiate movement by remodeling the ECM to create a low-resistance invasion path for follower cells.⁴³ Attachment to and detachment from ECM components such as VN are essential for this process in some cancers, such as ovarian cancer.⁴⁴ Similarly, VN secretion is greater in the SK-N-BE (2) than in the SH-SY5Y cell line,²² which may confer an intrinsic difference in migration dynamics. The increased cluster size under CLG treatment in SK-N-BE (2) cells relative to untreated controls at 7 days of culture may be the result of transient anoikis resistance; this may not occur in SH-SY5Y cells, where decreased cluster size was instead observed. Differences in anoikis resistance and drug response have been reported in many cell lines such as pleural mesothelioma, where the lack of CLG effect in anoikis-resistant cells points to anoikis susceptibility as a prerequisite for CLG-induced growth inhibition and migration.⁴⁵ An alternative explanation for the increased cluster size under CLG treatment in SK-N-BE (2) cells may be the higher number of cells remaining inside the clusters due to decreased migration activity to other hydrogel locations. It is interesting to note that exogenously cross-linked VN accentuated these effects, particularly in SK-N-BE (2) cells, suggesting the possibility that integrin expression is increased after VN is added and therefore a greater number of CLG binding sites become available with a subsequent increased response to CLG.

By exploiting the advantages of combining 3D biomimetic GTA-sf hydrogels with digital holographic microscopy, this work has shown an enhanced growth rate in both HR-NB cell lines with VN, pointing to this glycoprotein as a relevant prognostic predictor in HR-NB. In addition, the observed differences in cluster size between cell lines after CLG treatment are key to shedding light on the response that HR-NB patients may encounter and therefore are paramount for guiding patient selection and optimal timing of mechanotherapy.

Limitations of the study

Although the use of digital holography has permitted a more thorough assessment of cell and cluster growth dynamics, the exact molecular mechanisms underlying the observed effects are still not fully understood. This highlights a need for future studies in immunohistochemically stained GTA-sf hydrogel sections with proliferation and survival biomarkers such as ki67 and BCL2^{46,47} and VN secretion profiles. Furthermore, additional experiments with a greater number of cell lines, including those derived from patients and patient-derived xenografts, are necessary to guarantee the methodology's broad applicability and to enhance the value of the presented work. Given the restrictions on image acquisition with digital holography on larger imaging objects, the use of formalin-fixed paraffin-embedded (FFPE) GTA-sf hydrogel sections may also allow us to assess VN and other anchorage glycoproteins as well as the effect of CLG treatment over 10 days culture. Finally, integrating live imaging and digital pathology analyses with genomic strategies such as next-generation sequencing⁴⁸ and gene expression profiling (high throughput genomic [HTG] EdgeSeq) tools can help obtain a complete understanding of NB cell behavior in these contexts.

RESOURCE AVAILABILITY

Lead contact

Requests for further information and resources should be directed to and will be fulfilled by the lead contact, Rosa Noguera (rnoguera@uv.es).

Materials availability

This study did not generate new unique reagents.

Data and code availability

- All data reported in this paper will be shared by the [lead contact](#) upon request.
- This paper does not report original code.
- Any additional information required to reanalyze the data reported in this paper is available from the [lead contact](#) upon request.

ACKNOWLEDGMENTS

The authors gratefully acknowledge funding support from ISCIII and FEDER (European Regional Development Fund), grant number PI20/01107, FNB (Fundación Neuroblastoma), grant number PRV/00166 and CIBERONC (contract CB16/12/00484) to R.N. and thank Kathryn Davies for English corrections.

AUTHOR CONTRIBUTIONS

Conceptualization: S.G.-A. and R.N. Methodology: S.G.-A., I.V.-M., A.L.-C., S.N., and R.N. Investigation: S.G.-A. and I.V.-M. Funding acquisition: R.N. Supervision: S.G.-A. and R.N. Writing – original draft: S.G.-A. and R.N. Writing – review and editing: all authors have read and agreed to the final version of the manuscript.

DECLARATION OF INTERESTS

The authors declare no competing interests.

STAR★METHODS

Detailed methods are provided in the online version of this paper and include the following:

- KEY RESOURCES TABLE
- EXPERIMENTAL MODEL AND STUDY PARTICIPANT DETAILS
 - Cell lines
- METHOD DETAILS
 - Gelatin/silk-fibroin (GTA-sf) 3D hydrogel fabrication
 - Live cell imaging
- QUANTIFICATION AND STATISTICAL ANALYSIS
 - Statistical analysis

SUPPLEMENTAL INFORMATION

Supplemental information can be found online at <https://doi.org/10.1016/j.isci.2024.111231>.

Received: May 3, 2024

Revised: August 26, 2024

Accepted: October 21, 2024

Published: October 23, 2024

REFERENCES

1. Matthay, K.K., Maris, J.M., Schleiermacher, G., Nakagawara, A., Mackall, C.L., Diller, L., and Weiss, W.A. (2016). Neuroblastoma. *Nat. Rev. Dis. Prim.* 2, 16078.
2. Tolbert, V.P., and Matthay, K.K. (2018). Neuroblastoma: Clinical and biological approach to risk stratification and treatment. *Cell Tissue Res.* 372, 195–209.
3. Zafar, A., Wang, W., Liu, G., Wang, X., Xian, W., McKeon, F., Foster, J., Zhou, J., and Zhang, R. (2021). Molecular targeting therapies for neuroblastoma: Progress and challenges. *Med. Res. Rev.* 41, 961–1021.
4. Ward, E., DeSantis, C., Robbins, A., Kohler, B., and Jemal, A. (2014). Childhood and adolescent cancer statistics, 2014. *CA A Cancer J. Clin.* 64, 83–103.
5. Park, J.R., Bagatell, R., London, W.B., Maris, J.M., Cohn, S.L., Mattay, K.K., and Hogarty, M.; COG Neuroblastoma Committee (2013). Children’s oncology group’s 2013 blueprint for research: Neuroblastoma. *Pediatr. Blood Cancer* 60, 985–993.
6. Pickup, M.W., Mouw, J.K., and Weaver, V.M. (2014). The extracellular matrix modulates the hallmarks of cancer. *EMBO Rep.* 15, 1243–1253.
7. Anderson, N.M., and Simon, M.C. (2020). The tumor microenvironment. *Curr. Biol.* 30, R921–R925.
8. Discher, D.E., Janmey, P., and Wang, Y-I (2005). Tissue cells feel and respond to the stiffness of their substrate. *Science* 310, 1139–1143.
9. Schwartz, I., Seger, D., and Shaltiel, S. (1999). Vitronectin. *Int. J. Biochem. Cell Biol.* 31, 539–544.
10. Ishikawa-Sakurai, M., and Hayashi, M. (1993). Two collagen-binding domains of vitronectin. *Cell Struct. Funct.* 18, 253–259.
11. Preissner, K.T. (1991). Structure and biological role of vitronectin. *Annu. Rev. Cell Biol.* 7, 275–310.
12. Seiffert, D. (1997). Constitutive and regulated expression of vitronectin. *Histol. Histopathol.* 12, 787–797.
13. Dimova, T., Georgieva, R., Petlov, D., and Lazarova, S. (2005). Comparative study on the expression of fibronectin, vitronectin, alpha5beta1, beta3 and alphav integrins in goat and pig adrenal glands. *COMPTEs RENDUS-ACADEMIE BULGARE DES SCIENCES* 58, 1457.
14. Aaboe, M., Offersen, B.V., Christensen, A., and Andreasen, P.A. (2003). Vitronectin in human breast carcinomas. *Biochim. Biophys. Acta* 1638, 72–82.
15. Hao, W., Zhang, X., Xiu, B., Yang, X., Hu, S., Liu, Z., Duan, C., Jin, S., Ying, X., Zhao, Y., et al. (2016). Vitronectin: A promising breast cancer serum biomarker for early diagnosis of breast cancer in patients. *Tumour Biol.* 37, 8909–8916.
16. Chen, M.-H., Lu, C., Sun, J., Chen, X.-D., Dai, J.-X., Cai, J.-Y., and Chen, X.-L. (2016). Diagnostic and prognostic value of serum vitronectin levels in human glioma. *J. Neurol. Sci.* 371, 54–59.
17. Uhm, J.H., Dooley, N.P., Kyritsis, A.P., Rao, J.S., and Gladson, C.L. (1999). Vitronectin, a glioma-derived extracellular matrix protein, protects tumor cells from apoptotic death. *Clin. Cancer Res.* 5, 1587–1594.
18. Heyman, L., Leroy-Dudal, J., Fernandes, J., Seyer, D., Dutoit, S., and Carreiras, F. (2010). Mesothelial vitronectin stimulates migration of ovarian cancer cells. *Cell Biol. Int.* 34, 493–502.
19. Tas, F., Karabulut, S., Bilgin, E., Tastekin, D., and Duranyildiz, D. (2014). Clinical significance of serum fibronectin and vitronectin levels in melanoma patients. *Melanoma Res.* 24, 475–479.
20. Edwards, S., Lalor, P.F., Tuncer, C., and Adams, D.H. (2006). Vitronectin in human hepatic tumours contributes to the recruitment of lymphocytes in an alpha v beta3-independent manner. *Br. J. Cancer* 95, 1545–1554.
21. Tomasini-Johansson, B.R., Sundberg, C., Lindmark, G., Gailit, J.O., and Rubin, K. (1994). Vitronectin in colorectal adenocarcinoma—synthesis by stromal cells in culture. *Exp. Cell Res.* 214, 303–312.
22. Burgos-Panadero, R., Noguera, I., Cañete, A., Navarro, S., and Noguera, R. (2019). Vitronectin as a molecular player of the tumor microenvironment in neuroblastoma. *BMC Cancer* 19, 479.
23. Saraswathibhatla, A., Indana, D., and Chaudhuri, O. (2023). Cell–extracellular matrix mechanotransduction in 3d. *Nat. Rev. Mol. Cell Biol.* 24, 495–516.
24. López-Carrasco, A., Vieco-Martí, I., Granados-Aparici, S., Acevedo-León, D., Estañ-Capell, N., Portugal, R., Huerta-Aragón, J., Cañete, A., Navarro, S., and

- Noguera, R. (2024). Vitronectin levels in plasma of neuroblastoma patients and culture media of 3D models: A prognostic circulating biomarker? *Int. J. Mol. Sci.* **25**, 8733.
25. Chinot, O.L. (2014). Cilengitide in glioblastoma: When did it fail? *Lancet Oncol.* **15**, 1044–1045.
 26. Echavidre, W., Picco, V., Faraggi, M., and Montemagno, C. (2022). Integrin- $\alpha v \beta 3$ as a therapeutic target in glioblastoma: Back to the future? *Pharmaceutics* **14**, 1053.
 27. Yamada, S., Bu, X.Y., Khankaldyyan, V., Gonzales-Gomez, I., McComb, J.G., and Laug, W.E. (2006). Effect of the angiogenesis inhibitor cilengitide (emd 121974) on glioblastoma growth in nude mice. *Neurosurgery* **59**, 1304–1312.
 28. Horwacik, I., and Rokita, H. (2017). Modulation of interactions of neuroblastoma cell lines with extracellular matrix proteins affects their sensitivity to treatment with the anti-gd2 ganglioside antibody 14g2a. *Int. J. Oncol.* **50**, 1899–1914.
 29. Leblond, P., Dewitte, A., Le Tinier, F., Bal-Mahieu, C., Baroncini, M., Sarrazin, T., Lartigau, E., Lansiaux, A., and Meignan, S. (2013). Cilengitide targets pediatric glioma and neuroblastoma cells through cell detachment and anoikis induction. *Anti Cancer Drugs* **24**, 818–825.
 30. Burgos-Panadero, R., El Moukhtari, S.H., Noguera, I., Rodríguez-Nogales, C., Martín-Vañó, S., Vicente-Munuera, P., Cañete, A., Navarro, S., Blanco-Prieto, M.J., and Noguera, R. (2021). Unraveling the extracellular matrix-tumor cell interactions to aid better targeted therapies for neuroblastoma. *Int. J. Pharm.* **608**, 121058.
 31. Monferrer, E., Martín-Vañó, S., Carretero, A., García-Lizarribar, A., Burgos-Panadero, R., Navarro, S., Samitier, J., and Noguera, R. (2020). A three-dimensional bioprinted model to evaluate the effect of stiffness on neuroblastoma cell cluster dynamics and behavior. *Sci. Rep.* **10**, 6370.
 32. Monferrer, E., Dobre, O., Trujillo, S., González Oliva, M.A., Trubert-Panelli, A., Acevedo-León, D., Noguera, R., and Salmeron-Sanchez, M. (2022). Vitronectin-based hydrogels recapitulate neuroblastoma growth conditions. *Front. Cell Dev. Biol.* **10**, 988699.
 33. Sakai, S., Hirose, K., Taguchi, K., Ogushi, Y., and Kawakami, K. (2009). An injectable, in situ enzymatically gellable, gelatin derivative for drug delivery and tissue engineering. *Biomaterials* **30**, 3371–3377.
 34. Langhans, S.A. (2018). Three-dimensional in vitro cell culture models in drug discovery and drug repositioning. *Front. Pharmacol.* **9**, 6.
 35. Hellesvik, M., Øye, H., and Aksnes, H. (2020). Exploiting the potential of commercial digital holographic microscopy by combining it with 3d matrix cell culture assays. *Sci. Rep.* **10**, 14680.
 36. Kim, J., and Lee, S.J. (2024). Digital in-line holographic microscopy for label-free identification and tracking of biological cells. *Mil. Med. Res.* **11**, 38.
 37. Stoks, M., Vieco-Martí, I., Noguera, I., Sánchez-Sánchez, M., Burgos-Panadero, R., Navarro, S., and Noguera, R. (2023). Digital image analysis workflows for evaluation of cell behavior and tumor microenvironment to aid therapeutic assessment in high-risk neuroblastoma. *Comput. Biol. Med.* **164**, 107364.
 38. Silginer, M., Weller, M., Ziegler, U., and Roth, P. (2014). Integrin inhibition promotes atypical anoikis in glioma cells. *Cell Death Dis.* **5**, e1012.
 39. Goyal, U., and Ta, M. (2020). A novel role of vitronectin in promoting survival of mesenchymal stem cells under serum deprivation stress. *Stem Cell Res. Ther.* **11**, 181.
 40. Bae, H.-B., Zmijewski, J.W., Deshane, J.S., Zhi, D., Thompson, L.C., Peterson, C.B., Chaplin, D.D., and Abraham, E. (2012). Vitronectin inhibits neutrophil apoptosis through activation of integrin-associated signaling pathways. *Am. J. Respir. Cell Mol. Biol.* **46**, 790–796.
 41. Kim, Y.N., Koo, K.H., Sung, J.Y., Yun, U.J., and Kim, H. (2012). Anoikis resistance: An essential prerequisite for tumor metastasis. *Int. J. Cell Biol.* **2012**, 306879.
 42. Simpson, C.D., Anyiwe, K., and Schimmer, A.D. (2008). Anoikis resistance and tumor metastasis. *Cancer Lett.* **272**, 177–185.
 43. Vilchez Mercedes, S.A., Bocci, F., Levine, H., Onuchic, J.N., Jolly, M.K., and Wong, P.K. (2021). Decoding leader cells in collective cancer invasion. *Nat. Rev. Cancer* **21**, 592–604.
 44. Schneider, G., Suszyska, M., Kakar, S., and Ratajczak, M.Z. (2016). Vitronectin in the ascites of human ovarian carcinoma acts as a potent chemoattractant for ovarian carcinoma: Implication for metastasis by cancer stem cells. *J. Cancer Stem Cell Res.* **4**, e1005.
 45. Cheng, N.C., van Zandwijk, N., and Reid, G. (2014). Cilengitide inhibits attachment and invasion of malignant pleural mesothelioma cells through antagonism of integrins $\alpha v \beta 3$ and $\alpha v \beta 5$. *PLoS One* **9**, e90374.
 46. Li, L.T., Jiang, G., Chen, Q., and Zheng, J.N. (2015). Ki67 is a promising molecular target in the diagnosis of cancer (review). *Mol. Med. Rep.* **11**, 1566–1572.
 47. Qian, S., Wei, Z., Yang, W., Huang, J., Yang, Y., and Wang, J. (2022). The role of bcl-2 family proteins in regulating apoptosis and cancer therapy. *Front. Oncol.* **12**, 985363.
 48. López-Carrasco, A., Martín-Vañó, S., Burgos-Panadero, R., Monferrer, E., Berbegall, A.P., Fernández-Blanco, B., Navarro, S., and Noguera, R. (2020). Impact of extracellular matrix stiffness on genomic heterogeneity in mycn-amplified neuroblastoma cell line. *J. Exp. Clin. Cancer Res.* **39**, 226.
 49. Otte, J., Dyberg, C., Pepich, A., and Johnsen, J.I. (2020). Mycn function in neuroblastoma development. *Front. Oncol.* **10**, 624079.
 50. Trigg, R.M., and Turner, S.D. (2018). Alk in neuroblastoma: Biological and therapeutic implications. *Cancers* **10**, 113.
 51. Hasturk, O., Jordan, K.E., Choi, J., and Kaplan, D.L. (2020). Enzymatically crosslinked silk and silk-gelatin hydrogels with tunable gelation kinetics, mechanical properties and bioactivity for cell culture and encapsulation. *Biomaterials* **232**, 119720.

STAR★METHODS

KEY RESOURCES TABLE

REAGENT or RESOURCE	SOURCE	IDENTIFIER
Chemicals, peptides, and recombinant proteins		
Gelatin from porcine skin	Sigma-Aldrich	G2500
2-(N-morpholino) ethane sulfonic acid	Sigma-Aldrich	M3671
Tyramine	Sigma-Aldrich	T2879-5G
Carbodiimide hydrochloride	Sigma-Aldrich	03450
N-hydroxysuccinimide	Sigma-Aldrich	130672
Horseradish peroxidase	Sigma-Aldrich	P8375
Silk fibroin solution	Sigma-Aldrich	5154
Recombinant vitronectin	PrepoTech	AF-140-09
Cilengitide	Sigma-Aldrich	SML1594
Experimental models: Cell lines		
SK-N-BE (2) cells	ATCC	CRL-2271
SH-SY5Y cells	ATCC	CRL-2266
Software and algorithms		
App Suite 4.0.1	Phase Holographic Imaging PHI AB	https://phiab.com/holomonitor/cell-imaging-software/
GraphPad Prism 8.0.1	GraphPad	https://www.graphpad.com/

EXPERIMENTAL MODEL AND STUDY PARTICIPANT DETAILS

Cell lines

MYCN-amplified SK-N-BE (2) and ALK-mutated SH-SY5Y human NB cell lines were chosen from a variety of available cell lines, since MYCN-amplified and ALK-mutated tumors represent 64% of high-risk neuroblastoma [50 and 14%, respectively].^{49,50} Cells were acquired from American Type Culture Collection (ATCC, Manassas, VA, USA) and cultured in IMDM medium (Gibco, Life Technologies, Waltham, MA, USA) supplemented with 10% FBS, 1% insulin/transferrin and 1% Penicillin/streptomycin at 37°C in 5% CO₂ atmosphere. Two-dimensional (2D) cell cultures were grown in T75 flasks until they reached 80% confluence for 3D-hydrogel fabrication. Cell line authentication was performed by assessing morphology and growth rate on a Leica Inverted Phase Contrast microscope and genetic profile was confirmed by using Fluorescence *in situ* hybridization (FISH) and single nucleotide polymorphism (SNP) array before conducting the experiments. To prevent and control for mycoplasma contamination, 0.2% Plasmocin (InvivoGen) was added to the culture medium and tested with the Rapid Mycoplasma Detection Kit (AssayGenie) after the cells were thawed and frozen for long-term storage.

METHOD DETAILS

Gelatin/silk-fibroin (GTA-sf) 3D hydrogel fabrication

First, tyramine-modified gelatin (GTA) was obtained as previously described (Shinji Sakai et al., 2009). Briefly, gelatin (Sigma-Aldrich, St. Louis, MO) was melted in 50 mL of 0.05 M 2-(N-morpholino) ethane sulfonic acid buffer at 60°C and then 500 mg of tyramine (Sigma-Aldrich, St. Louis, MO) was added after the temperature reached 25°C the carbodiimide-mediated reaction was facilitated by adding 184 mg of carbodiimide hydrochloride (EDC) and 57 mg of N-hydroxysuccinimide (NHS) to obtain GTA after 18 h of agitation at room temperature, followed by dialysis in 3.5 MWCO membrane in distilled water and lyophilization. Once ready, GTA was kept at –20°C until use.

Hydrogels were built modifying a previously reported protocol⁵¹ with double amount (20U/ml) of horseradish peroxidase (HRP). Briefly, the necessary amount to obtain 1% GTA was weighted, UV-sterilized for 10 min and mixed with serum-free cultured medium to dissolve at 50°C. Once dissolved, the necessary amount of silk fibroin (sf) was added to obtain a final composition of 3% SF. In hydrogels containing VN, 400 µg/mL of recombinant VN (PrepoTech, London, UK) was added. After trypsinizing and counting live cells using a TC20 automated cell counter (BIO-RAD), cells were resuspended in serum-free culture medium and then added to the GTA-sf solution. Approximately 120,000 cells were used per hydrogel. Drops of HRP and H₂O₂ (1,25 and 2µL, respectively) were added to each 24-well plate well and approximately 60µL drops of the GTA-sf cell solution were added gently on top. Hydrogels were allowed to gelify at 37°C for 1 h followed by the addition of 1–2 mL supplemented medium. Hydrogels were kept at 37°C with medium changes every two-three days, with and without the addition of CLG (100µM). Cell cluster growth within hydrogels was assessed during 24 h at days 3, 7 and 10 of culture inside an incubator at 37°C in 5%

CO₂. Four groups were obtained in total: hydrogels without VN added (non-VN-added), containing cell-secreted VN only, hydrogels with VN added (VN-rich), hydrogels without VN added and CLG (non-VN-added-CLG) and hydrogels with VN added and CLG (VN-rich CLG).

Live cell imaging

Cell cluster growth, morphology and movement were assessed with the Holomonitor M4 live cell imaging system from Phase Holographic Imaging (Lund, Sweden). Before monitoring, a capture pattern of focus positions was selected for each well and time lapse imaging was set to acquire one image every 15 min over specific periods of time. To assess cell cluster growth in 2D, a total of 17 images spanning 1 h and 15 min were extracted from a single focus position of control and CLG-treated groups. To evaluate cluster growth embedded in the hydrogel border, a total of 72 images were analyzed for each NB cell line, corresponding to frames 0 h and 24 h of each of the three focus positions in all groups. For cell cluster growth assessment in 2D at the hydrogel border, a total of 17 images spanning 1 h and 15 min were selected from each of the three focus positions in all groups. The total number of clusters analyzed is shown in [Figure S2B](#). Time lapse image quantification was carried out using parameters of App Suite, a software system provided by the Holomonitor M4 designed for reconstruction and analysis of the holographic microscopy images of unlabeled cells. For automated cell/cluster tracking, the same settings and thresholds were used for all groups. The following parameters were evaluated: "Optical volume (μm^3)", which represents single cell/cluster volume and is calculated from the phase shift, irrespective of cell/cluster shape; and "optical thickness (μm)", representing the maximum thickness obtained from the phase shift and independently of cell/cluster shape and irregularity, which measures the degree of deviation of the cell/cluster circumference from the circumference of a perfect circle. The value 0 indicates a circular cell/cluster, approaching 1 when the irregular outline of the cell/cluster increases. To monitor and depict the movement of cell clusters, single cell X-Y position plots were used to show overall cell migration trajectory (μm). The Export Movie module was used to generate approximately 60 MB movies, using 6 frames per second (fps).

QUANTIFICATION AND STATISTICAL ANALYSIS

Statistical analysis

Data are presented as mean \pm standard error of mean (SEM) and were analyzed and represented using GraphPad Prism 8.0.1 software. Statistical significance was evaluated using non-parametrical Kruskal Wallis with Dunn's test for multiple comparisons between groups.